Silicon (2024) 16:3257–3265
https://doi.org/10.1007/s12633-024-02905-0

RESEARCH

Optimization of Process Parameters for Silicon Casting Manufacturing Using Fully Transient 3D Modeling Approach

Amir Reza Ansari Dezfoli[1]

Received: 14 December 2023 / Accepted: 4 February 2024 / Published online: 23 February 2024

Abstract
During the last three years, the world experienced a silicon-wafer shortage due to the COVID-19 pandemic and competition for technology between different countries. Direct silicon casting could be the solution for this issue because of low operation costs and ease of production. In this study, the direct casting of silicon was simulated using a fully transient three-dimensional model including the energy equation, Naiver-Stokes equations, moving mesh theory, and thermal stress equations. The heater power ratios and speed of the side insulation wall were considered as major parameters during the casting. To evaluate the simulation, the crystal-front shape and heater power were validated using experimental results. The simulation results show that by increasing the side heater power, the crystal-front shape changed from concave to almost flat or slightly convex. Additionally, the thermal stress can be decreased about 19% by altering the side heater power. The speed of the side insulation wall was found to have great effect on the casting speed, but the effect of the crystal-front shape was minor.

Keywords Silicon casting manufacturing · Direct casting · Silicon ingot · Crystal growth · Thermal stress

1 Introduction

While monocrystalline silicon currently dominates the materials used in the photovoltaic and solar panel industry, multi-crystalline silicon wafers remain popular in this field due to their cost-effectiveness and efficient throughput. [1–3]. Therefore, improving the casting process of multi-crystalline silicon is attractive for many producers for manufacturing a silicon wafer at lower cost but with higher efficiency [4–6].

Direct casting is known as one of the most effective casting processes to make a silicon ingot because the final product has most of the favorable properties of a silicon wafer for solar cell applications with low cost [7, 8]. The main difficulty in producing the silicon ingot is producing a dislocation-free ingot [3, 9]. Dislocation is the most important defect for the carrier lifetime and solar-cell efficiency. Dislocations are initiated near the solid-liquid interface during the crystal growth process [10–12]. The energy of dislocation formation comes from thermal stress at the crystal front (solid-melt interface). After forming, the dislocations propagate into the formed crystal and ruin the silicon ingot. To avoid dislocation formation, the crystal-front shape, heat flux at the crystal front, and cooling rate of the ingot should be controlled [9, 13]. Helmreich [3] discussed the different approaches in both chemical preparation and special crystallization techniques related to dislocation propagation and the problem of solar-grade quality. Fujiwara et al. [13] investigated the growth of structure-controlled polycrystalline silicon ingots for solar cells by a casting method using carbon-coated silica crucibles with various inner shapes. They demonstrated that the crucible shape can influence the grain orientation and size distribution of the ingot and that a hexagonal crucible can produce a quasi-single-crystal ingot with high conversion efficiency. He et al. [10] investigated the effects of an octagonal thermal field on the quality of a multi-crystalline silicon ingot. They found that the octagonal thermal field can reduce the temperature gradient, cooling rate, and impurity concentration in the melt and improve the grain size, grain boundary angle, dislocation density, and resistivity distribution of the ingot. Lau et al. [11] showed that silicon carbide can reduce the nucleation undercooling and promote the formation of large grains with uniform orientation on the wafer surface. Su et al. [14] designed and optimized a spray-type gas guidance system (GGS) to reduce

✉ Amir Reza Ansari Dezfoli
AmirAnsari@ncut.edu.tw

[1] Department of Intelligent Automation Engineering, National Chin-Yi University of Technology, Taichung, Taiwan, Republic of China

the impurities in a silicon casting furnace by using 3D global simulations and an orthogonal experiment. They showed that the GGS can decrease the area-average concentration of CO at the melt free surface by 31% and weaken the kinetic rate of reaction at the cover. They also found that the optimal GGS parameters were an argon flow rate of 40 L/min, deflector length of 50 mm, and distance between the GGS and melt free surface of 50 mm. Yuan et al. [9] analyzed the dislocation propagation in Si wafers during a Si-IGBT fabrication process using X-ray topography and numerical simulation. They confirmed that a lower-temperature process causes smaller dislocation propagation in Si wafers by calculating the dislocation density during the diffusion process with different temperatures and times.

Nagarajan et al. [15] conducted a numerical simulation to explore the effects of introducing an insulation block into multicrystalline silicon direct casting. They reported that modifying the direct casting process can lead to a reduction in power consumption and an improvement in ingot quality. Kesavan et al. [16] conducted a numerical investigation into the crystal front shape and carbon impurity during directional casting. Their findings revealed that the design of the heater significantly influences the crystal front shape and can also impact impurity concentration during the casting process. This study conclusively demonstrated that the positioning of process heat has a direct impact on the ultimate quality of the final product. Srinivasan et al. [17] employed a transient global heat transfer model to investigate the use of a bottom grooved directional solidification (DS) furnace. The objective of the study was to assess the performance of replacing the initial seed with a bottom grooved pattern. The results indicated that the bottom grooved approach, with a size of 60 mm, exhibited superior performance compared to the conventional direct casting method. Sugunraj et al. [18] utilized the finite volume method to optimize multicrystalline silicon crystal growth, incorporating a bottom helium gas retort modification. Their study successfully demonstrated that the proposed modified silicon casting can reduce SiC formation and dislocation density. Keerthivasan et al. [19] endeavored to optimize the silicon casting process through retort modification. They constructed a 2D axisymmetric model to examine radiation heat transfer and impurity distribution during direct casting. Their findings provided evidence that the modified retort contributes to an improvement in the final ingot quality. In a separate study, Keerthivasan et al. [20] introduced a modified furnace model for multi-crystal silicon casting. They implemented a partial replacement of the bottom susceptor with the aim of controlling the crystal front shape and temperature. Numerical simulations demonstrated that this modification resulted in reduced power consumption and improved ingot quality.

The aim of this study was to investigate the direct casting of silicon using a fully transient three-dimensional model that couples the energy equation, Navier-Stokes equations, moving mesh theory, and thermal stress equations. The model was validated by comparing the simulated results with experimental data on the crystal-front shape and heater power. The main process parameters considered in this study were the heater power ratios and the speed of the side insulation wall, which were varied to analyze their effects on the casting speed, crystal-front shape, thermal stress, and impurity distribution in the silicon ingot. The results of this study could provide valuable guidance for improving the efficiency and quality of the direct casting of silicon for solar cell applications.

2 Method and Modeling

A direct casting furnace is illustrated in Fig. 1. The initial silicon chunks are located at the bottom of the quartz crucible, which is filled with raw silicon materials. The crucible is located inside a graphite container in the center of the furnace.

Argon gas flows inside the furnace during the process to remove impurities from the furnace atmosphere. Two types of heaters heat the top and side areas of the crucible. The power and amount of heat generated by the heaters can be set separately. There is an insulation wall that separates the heating area and the steel wall of the furnace. The steel wall is cooled using cooling water. The side insulation can move vertically.

After the initial setup, the heaters starts to heat the system, and the melting stage starts. The meting process continues until the initial raw materials and a part of initial silicon chunk partially melt. Afterward, the

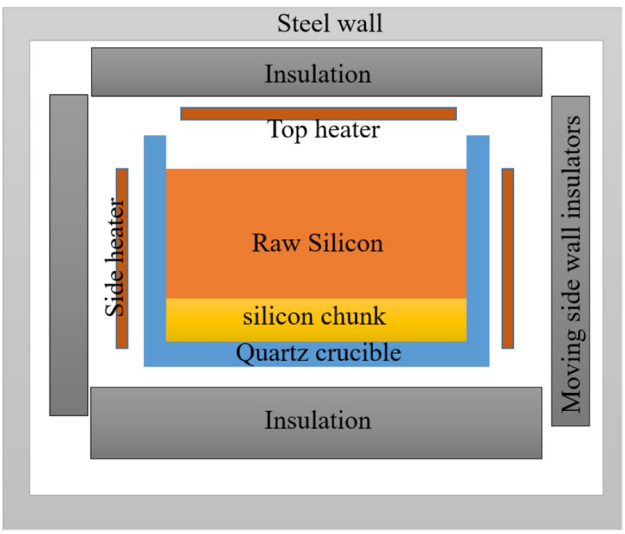

Fig. 1 Diagram of direct silicon casting

directional solidification starts using decreasing heater powers and also by moving side insulation wall upside. In this condition, the directional solidification starts from the bottom area of the crucible and continues to the top side.

The governing equations are [4, 22]:

$$\frac{\partial T}{\partial t}+v_r\frac{\partial T}{\partial r}+v_z\frac{\partial T}{\partial z}+\frac{v_\varphi}{r}\frac{\partial T}{\partial \varphi}=\alpha\left(\frac{1}{r}\frac{\partial}{\partial r}\left(r\frac{\partial T}{\partial r}\right)+\frac{1}{r^2}\frac{\partial^2 T}{\partial \varphi^2}+\frac{\partial^2 T}{\partial z^2}\right)+\frac{\dot{q}}{\rho c_p} \tag{1}$$

$$\rho\left(\frac{\partial u_r}{\partial t}+u_r\frac{\partial u_r}{\partial r}+\frac{u_\varphi}{r}\frac{\partial u_r}{\partial \varphi}+u_z\frac{\partial u_z}{\partial z}-\frac{{u_\varphi}^2}{r}\right)=\mu\left[\frac{1}{r}\frac{\partial}{\partial r}\left(r\frac{\partial u_r}{\partial r}\right)+\frac{1}{r^2}\frac{\partial^2 u_r}{\partial \varphi^2}+\frac{\partial^2 u_r}{\partial z^2}-\frac{u_r}{r^2}-\frac{2}{r^2}\frac{\partial u_\varphi}{\partial \varphi}\right] \tag{2}$$

$$\left(\frac{\partial u_\varphi}{\partial t}+u_r\frac{\partial u_\varphi}{\partial r}+\frac{u_\varphi}{r}\frac{\partial u_r}{\partial \varphi}+u_z\frac{\partial u_\varphi}{\partial z}+\frac{u_r u_\varphi}{r}\right)=\mu\left[\frac{1}{r}\frac{\partial}{\partial r}\left(r\frac{\partial u_\varphi}{\partial r}\right)+\frac{1}{r^2}\frac{\partial^2 u_\varphi}{\partial \varphi^2}+\frac{\partial^2 u_\varphi}{\partial z^2}-\frac{u_\varphi}{r^2}+\frac{2}{r^2}\frac{\partial u_\varphi}{\partial \varphi}\right] \tag{3}$$

$$\left(\frac{\partial u_z}{\partial t}+u_r\frac{\partial u_z}{\partial r}+\frac{u_z}{r}\frac{\partial u_z}{\partial \varphi}+u_z\frac{\partial u_z}{\partial z}\right)=-\frac{\partial P}{\partial z}+\mu\left[\frac{1}{r}\frac{\partial}{\partial r}\left(r\frac{\partial u_z}{\partial r}\right)+\frac{1}{r^2}\frac{\partial^2 u_z}{\partial \varphi^2}+\frac{\partial^2 u_z}{\partial z^2}\right]+\rho\beta(T-T_m)g_z \tag{4}$$

where T is the temperature, α is the thermal diffusivity, ρ is the density, c_p is the specific heat, and u_r, u_z, and u_φ are the melt velocity components in the r, z, and φ directions, respectively. β is the thermal expansion coefficient, μ is the silicon viscosity, T_m is the silicon melting temperature, and $\dot{q}$ is the heat generation, which is applied to just the top and side heaters.

At the interface between a liquid and solid,

$$\vec{V}=0. \tag{5}$$

At the silicon melt-argon interface, the tangential velocity component should satisfy the following conditions:

$$\mu_{InP}\frac{\partial u_{InP}}{\partial n}=\mu_{Ar}\frac{\partial u_{Ar}}{\partial n}, \tag{6}$$

where u is the tangential velocity component, and n is the normal direction of the free surface. At the solid joints, the thermal conditions between solid 1 and solid 2 are:

$$\lambda_1\frac{\partial T_1}{\partial n}=\lambda_2\frac{\partial T_2}{\partial n} \tag{7}$$

$$T_1=T_2. \tag{8}$$

Radiation heat transfer is also applied between all surfaces inside the furnace. The crystal-front shape is a function of the melt and crystal temperature gradient.

The moving mesh method was used to determine the crystal-front shape during the transient simulation. Based on this theory, at each time step, the movement of each mesh is calculated as [16]:

$$\Delta X=v_{growth}\Delta t. \tag{9}$$

v_{growth} is the growth velocity due to temperature gradient difference in the crystal and melt, which can be determined by [23]:

$$v_{growth}=\frac{k_s\nabla T_s-k_l\nabla T_l}{\rho_s\Delta H} \tag{10}$$

where ΔH denotes the solidification latent heat, and s and l denote the solid and liquid phases of silicon. The growth speed was set to 1 mm/min and was controlled using the heater powers.

The thermal elastic stress model is given by [24]:

$$\frac{1}{r}\frac{\partial\left(r\sigma_{rr}\right)}{\partial r}+\frac{\partial\sigma_{rz}}{\partial z}-\frac{\sigma_{\varphi\varphi}}{r}=0 \tag{11}$$

$$\frac{1}{r}\frac{\partial\left(r\sigma_{rz}\right)}{\partial r}+\frac{\partial\sigma_{zz}}{\partial z}=0, \tag{12}$$

where σ_{rr}, $\sigma_{\varphi\varphi}$, σ_{zz}, and σ_{rz} are the thermal stresses, and the stress-strain correlation can be explained by [24]:

$$\begin{pmatrix}\sigma_{rr}\\ \sigma_{\varphi\varphi}\\ \sigma_{zz}\\ \sigma_{rz}\end{pmatrix}=\begin{pmatrix}C_{11}&C_{12}&C_{13}&0\\ C_{12}&C_{22}&C_{13}&0\\ C_{13}&C_{13}&C_{33}&0\end{pmatrix}\begin{pmatrix}\varepsilon_{rr}-\alpha\left(T-T_m\right)\\ \varepsilon_{\varphi\varphi}-\alpha\left(T-T_m\right)\\ \varepsilon_{zz}-\alpha\left(T-T_m\right)\\ \varepsilon_{rz}\end{pmatrix} \tag{13}$$

Table 1 Material properties used in this study

Components	Silicon	Crucible Fused silica	Furnace walls	Heaters-Support plate Conductive Graphite
Density [kg/m^3]	2329	2190	160	430
Thermal conductivity [W/mK]	$562\,T^{-0.346}$	$6\times10^{-3}\,T+1.5$	$-2\times10^{-5}\,T^2+0.031\,T-13.744$	$4\times10^{-5}-0.107\,T+119.5$
Heat capacity [KJ/KgK]	$10^{-9}\,T^3-2^{-6}\,T^2+0.0009\,T+0.6938$	$-4\times10^{-7}\,T^2+7\times10^{-4}\,T+0.71$	$-3\times10^{-7}\,T^2+10^{-3}\,T+1.22$	$8\times10^{-4}\,T+1.6$
Emissivity	0.54	0.1	0.83	0.9
Viscosity [centipoise]	$-0.0006\,T+1.6334$	-	-	-
Melting temperature [K]	1685	-	-	-

where C_{ij} is the elastic constant,α is the thermal expansion coefficient, and ε_{ij} is strain. The crystal front is considered as a no-traction boundary ($\vec{\sigma}.\vec{n}=0$). Si's elastic constants C_{11}, C_{12}, and C_{44} and the thermal expansion are expressed as follows:

$$\begin{aligned} C_{11} &= 16.564\times10^{11}\exp\left(-9.4\times10^{-5}(T-298.15)\right)\\ C_{12} &= 6.394\times10^{11}\exp\left(-9.8\times10^{-5}(T-298.15)\right)\\ C_{44} &= 7.951\times10^{11}\exp\left(-8.3\times10^{-5}(T-298.15)\right) \end{aligned} \tag{14}$$

$$\begin{aligned} \alpha_1 &= 3.725\times10^{-6}\left(1.0-\exp\left(-5.88\times10^{-3}(T-124.0)\right)\right)\\ &\quad +5.84\times10^{-10}T \end{aligned} \tag{15}$$

All physical and materials properties used in this paper are listed in Table 1.

Before applying the model to optimize the crystal growth process, a simulation was performed for a real crystal growth process, and the heater power and crystal-front shape were compared between the simulation and an experiment. A crystal with a diameter and height of 1100 mm and 400 mm was grown in a direct casting furnace. The heater power ratio was set as 0.7:0.3, which means 70% of the total power was generated in the top heater, and the rest was provided by the side heater.

The side-insulation wall speed was kept at a constant value of 0.46 mm/min which corresponds with a total of 300 mm of displacement upwards during the casting. The crystal growth speed was set as 1 mm/min, and the argon gas pressure and volume were 15 Torr and 50 L/s, respectively. The furnace's outside walls were kept at 300K during the casting. The time step was limited and controlled by the Courant number [25].

A tetrahedral mesh with 98,000 nodes and 598,326 degrees of freedom was applied to the geometry. A mesh sensitivity analysis was performed, and the maximum mesh size was about 0.1 mm with a mesh growth rate of 0.9 and curvature factor of 0.3. The maximum time step was limited to keep the Courant number below 0.5. The type and material properties of the furnace have been described in previous studies [23, 25, 26].

3 Results and Discussion

The crystal growth took about 10.5 hours. The heater power was compared between the simulation and real process, as shown in Fig. 2. As shown in the figure, the total power was about 73 kW in the initial of process. When moving the side insulation, the crystallization started, and more power was needed to keep the top area of the crystal warm. In these conditions, the heater power increased to about 96 kW at the end of the process. The comparison showed good agreement

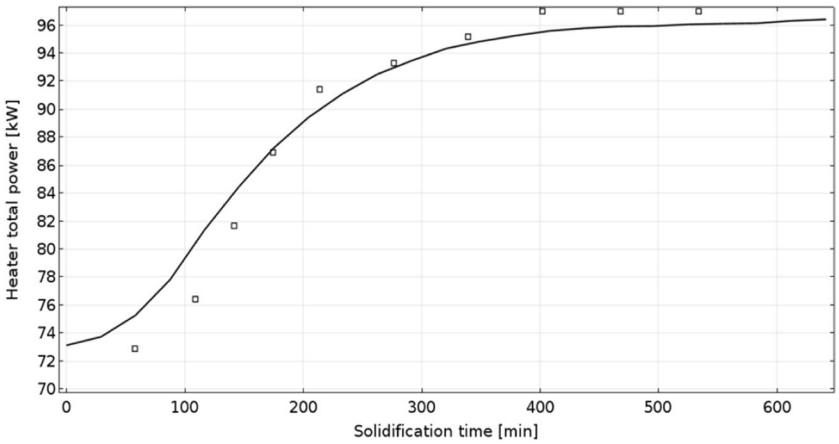

Fig. 2 Comparison of the total power for crystal growth between the simulation and experiment

between the simulation and real heater power. The maximum error was found to be about 3%.

To investigate the simulation model's accuracy, another experiment was performed to observe the crystal-front shape. In this experiment, the crystal growth was performed with the same conditions. After the crystal length reached 10 mm, the process was stopped, and the heaters were turned off. After cooling down the system, lifetime mapping was performed on the wafers obtained from the ingot, and the clear shape of the crystal front was obtained.

The crystal front was compared with the simulation and is illustrated in Fig. 3. The experimental data were acquired through a carrier lifetime map of a rapidly cooled ingot at a crystal length of 17 mm. The crystal front had a concave shape (toward crystal) in both the simulation and experimental results, which proves that the heat exits from the side wall faster, which is why the concave crystal-front shape was formed. The comparison showed good agreement between the simulation and experiment.

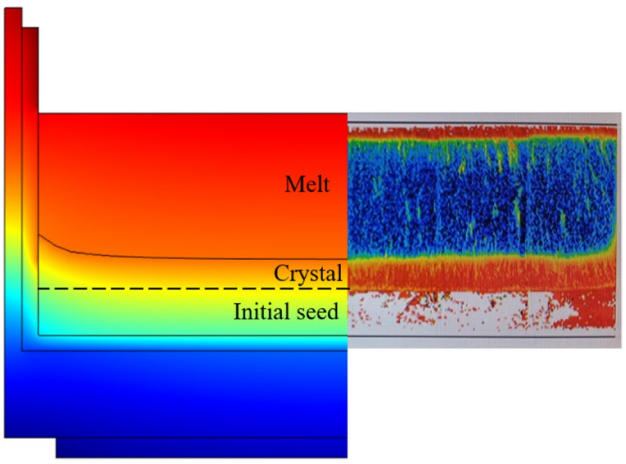

Fig. 3 Comparison of crystal-front shape between simulation (left) and experiment (right)

The temperature profile and melt-flow streamlines were studied for crystal lengths of 7 mm, 17 mm, 27 mm, 37mm and 47 mm. The results showed that by moving up the side insulation, directional casting started from the bottom region toward the top. There were two regions in the furnace: a top hot area and a cold bottom area. As the side insulation starts to move up, the heat exchange from the bottom of the crucible provides enough energy for crystal growth.

Additionally, the melt flow shows the formation of a big vortex inside the melt, which flows from the side to the center. This form of flow from the side to the center has a big role in forming the concave shape. During the solidification, the latent heat is released from the solid in the melt region near the solid-liquid interface. The flow from the side to the center moves the heat by convection from the side and transfers into the center regions. This helps to make the cooling rate faster at the side and forms a concave shape of the crystal front Fig. 4.

In order to optimize the silicon casting process and find the effect of different parameters on the process, side-wall speed and heater power ratio were changed, and their effect was investigated. The side-wall speed was changed from 0.23 to 0.46 mm/min. These speeds correspond to total upward movement of 150 and 300 mm during the casting process. Furthermore, the heat ratio between the top heater and side heater was changed from 0.7:0.3 to 0.5:0.5.

The crystal-front shapes corresponding to various conditions were calculated for crystal lengths of 7 mm, 17 mm, 27 mm, 37mm, and 47 mm, as illustrated in Fig. 5. The outcomes indicate that, for a heater ratio of 0.7:0.3, the crystal front exhibited a concave shape, and even with a change in side-wall speed from 0.23 mm/min to 0.46 mm/min, the concave crystal-front shape remained unchanged. The increased heat released at the top heater affected both higher heat radiation at the center and the formation of a hotter melt at the top center. When higher power was applied to the top heater, it resulted in an elevated temperature at the ingot center, causing the crystal front to adopt a more pronounced concave

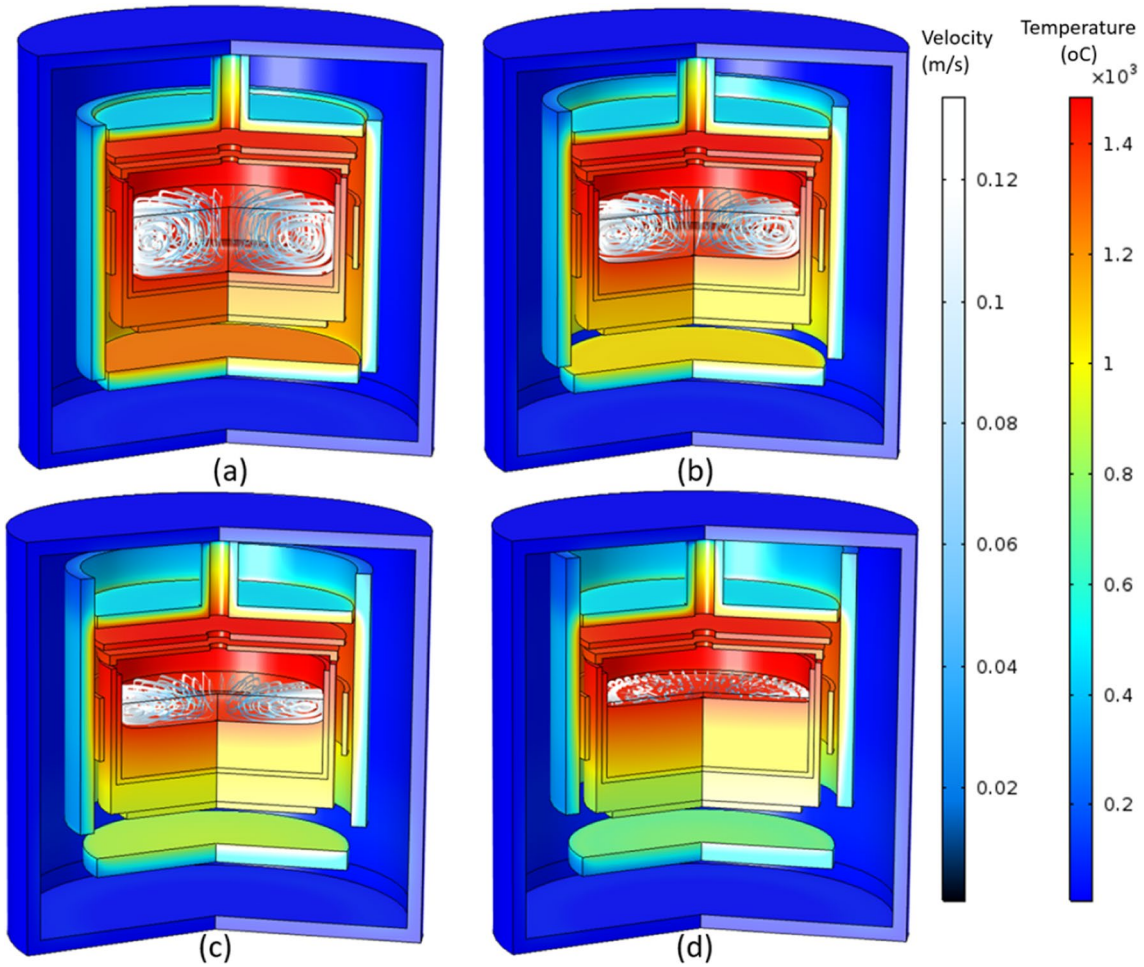

Fig. 4 The temperature profile and melt flow during the seeded-silicon direct casting for crystal lengths of (**a**) 7 mm, (**b**) 17 mm, (**c**) 27 mm, and (**d**) 37 mm

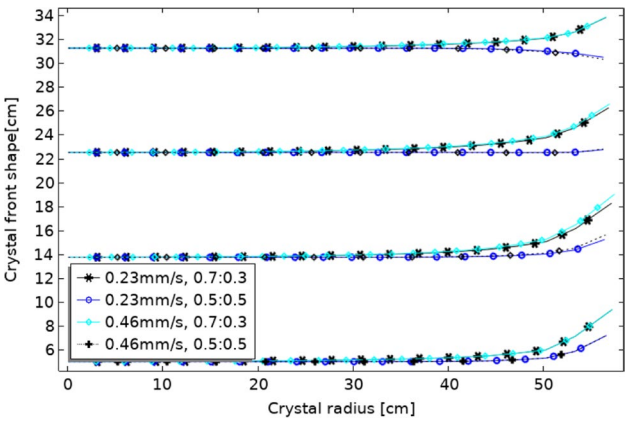

Fig. 5 The crystal-front shape during direct casting as a function of speed of the side insulation wall and top and side heater ratio

shape. At a small crystal length of 7 mm, the maximum crystal front depth was approximately 4.3 mm. In this scenario, the melt flow pattern, which removes released latent heat from the side to the center, led to faster crystal growth at the sides than at the center. This trend persisted until a crystal length of about 17 mm, where the maximum crystal deflection was around 4.2 mm. As the crystal length increased to approximately 27 mm, with less melt volume and a closer distance between the crystal front and top heater, the crystal concavity began to decrease to 3.1 mm, further reducing to 1.8 mm at crystal lengths of 27 mm and 37 mm. It seems that increasing the speed of the side insulation wall just decreases the concavity of the crystal-front shape. When decreasing the side insulation speed, less radiation heat exchange occurs between the side wall and the bottom cold area. This

decreases the cooling rate of the side wall and subsequently decreases the crystal-front shape's concavity because more uniform heat extraction happens from the center and side regions during the casting.

When the heater power ratio was more balanced at 0.5:0.5, a shift in the crystal-front shape became evident. Under this condition, the hotter side emerged, leading to a reduction in side growth rate and an overall loss of the concave shape in the crystal front. Specifically, at a crystal length of 7 mm, the large amount of melt and the lower location of the crystal front toward the side heater still allowed the melt flow to play a crucial role in removing released heat from the side into the center area. This resulted in the formation of a concave crystal front with a 2.1 mm concavity. As the crystal length increased to 17 mm, the crystal front moved closer to the side heater, receiving direct heat radiation from the side heater. This decrease in the side crystal growth rate led to the formation of a less concave crystal shape with a maximum crystal deflection of 1.5 mm. Finally, upon reaching a crystal length of 27 mm, the crystal front reached the hottest level of the side heater (heater center), resulting in the formation of a flat crystal front shape. At a longer crystal length of 37 mm, due to less melt volume and the warmer side heater in comparison to the 0.7:0.3 heater ratio, the crystal front adopted a flat shape with a small convexity.

Maintaining a flat or slightly concave crystal-front shape during casting proves beneficial in reducing thermal stress and preventing dislocation formation [23]. The configuration of the crystal-front is influenced by the heater power ratios,

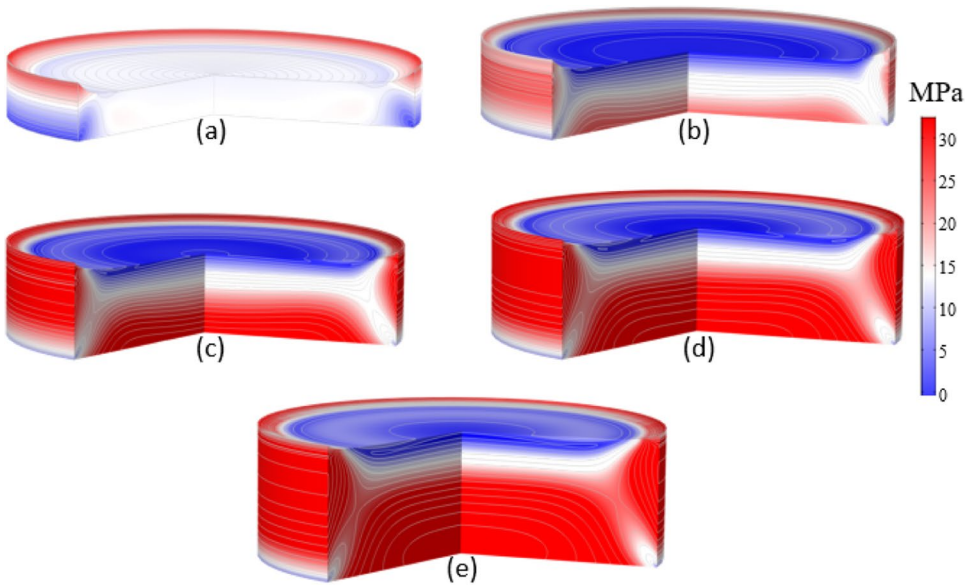

Fig. 6 The thermal stress distribution for a heater ratio of 0.7:0.3 for side wall speed of 0.46 mm/min and crystal lengths (**a**) 7 mm, (**b**) 17 mm, (**c**) 27 mm, (**d**) 37mm and (**e**) 47 mm

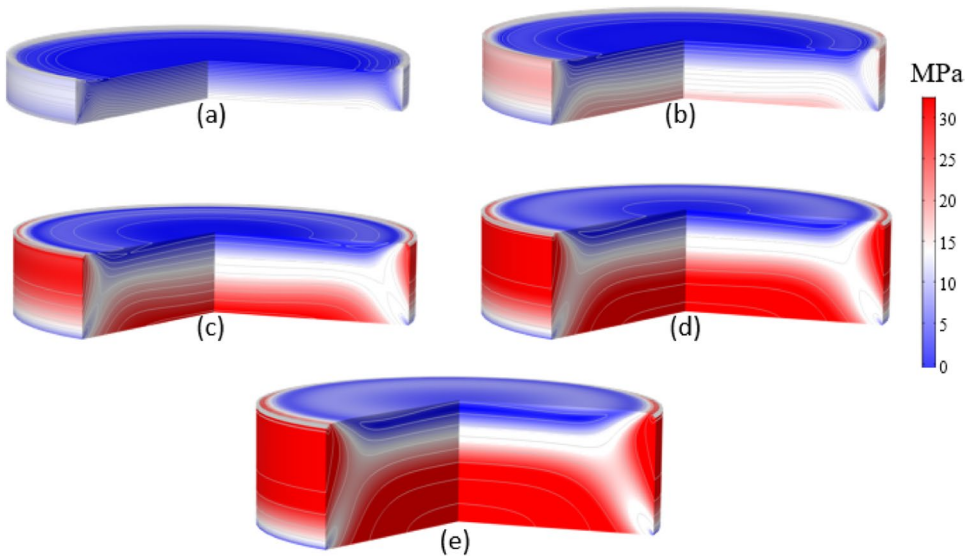

Fig. 7 The thermal stress distribution for heater ratio of 0.5:0.5 for side wall speed of 0.46 mm/min and crystal lengths of (**a**) 7 mm, (**b**) 17 mm, (**c**) 27 mm (**d**) 37 mm, and (**e**) 47mm

as heat is applied to different regions of the ingot. A higher top heater power than side heater power leads to a faster temperature decrease on the side walls compared to the central regions, resulting in a concave crystal-front shape. Conversely, providing more heat through the side heater raises the side wall temperature, evening out the solidification speed between the center and side regions. This condition fosters a more uniform solidification rate, yielding a flatter solid-liquid interface.

In order to evaluate the effect of the crystal-front shape and heater power ratio on thermal stress, the thermal stress was determined for two different heater ratios of 0.7:0.3 and 0.5:0.5 for a side wall speed of 0.46 mm/min, as shown in Figs. 6 and 7. The von Mises stress was chosen to evaluate the thermal stress. It revealed that the distribution of thermal stress was almost the same for both heater power ratios. The maximum thermal stress was located at the side wall and bottom center of the ingot.

The results revealed that the heater ratio has a great effect on the thermal stress during the directional casting. At 0.7:0.5, the maximum thermal stress was measured as 18.5 MPa, 21.7 MPa, 27.8 MPa, and 29 MPa at crystal lengths of 7 mm, 17 mm, 27 mm, and 37 mm, respectively. These values declined to 13.3 MPa, 15.1 MPa, 19.7 MPa, 23.9 MPa, and 24.8 MPa when the heater ratio changed to 0.5:0.5.

The thermal stress is a function of radial and axial temperature gradients. If larger heat is released from the top side, the radial temperature gradient increases and causes more thermal stress. When releasing equal heat from the top and side, more uniform cooling occurs in the crystal, and less thermal stress is generated. Additionally, the flatter form of the crystal front helps to reduce the thermal energy propagating into the crystal.

4 Conclusion

To avoid trial-and-error optimization during silicon casting, simulation can play an important role. A 3D transient model was implemented to study the effect of process parameters during the directional silicon casting. The heater power and side-wall insulator speeds are known as two important process parameters to control the final ingot quality. The simulation showed that both the crystal-front shape and thermal stress are strongly dependent on the heater power ratio. When providing more equal heat at the side and top heaters, the crystal-front shape changed from concave to almost flat or slightly concave. Furthermore, the thermal stress decreased when altering the heater power ratio from 0.7:0.3 to 0.5:0.5. On the other hand, the speed of the insulation side wall had less effect on casting.

The study focused on optimizing the crystal growth process in a direct casting furnace for silicon through the application of a comprehensive simulation model. This model delved into the intricate thermal and fluid dynamics that governed the growth, providing valuable insights into the effects of varying parameters. We aimed to fine-tune the distribution of heater power and the speed of the side-wall insulation to influence the crystal-front shapes and growth rates. The simulation not only helped understand the complexities of the process but also validated its accuracy by comparing results with experimental data. The overarching goal was to leverage these insights to enhance the real-world crystal growth process, minimize thermal stress, prevent defects, and ultimately improve the efficiency and quality of silicon crystal production for practical applications. The study contributed to a deeper understanding of the interplay between process variables and crystal quality, paving the way for optimized and high-quality crystal growth in industrial settings.

Acknowledgements Not applicable

Author's Contributions Amir R. A. Dezfoli did the conceptualization, investigation, methodology, project administration, resources, software, supervision, visualization, writing the original draft, review, and editing.

Funding This work was supported by the National Science and Technology Council of Taiwan [grant number NSTC: 112-2222-E-167 -001 -MY3].

Data Availability The data that support the findings of this study are available from the authors upon reasonable request.

Declarations

Competing Interests The authors declare no competing interests

Consent for Publication The Author confirms that the work described has not been published before and is not under consideration for publication elsewhere.

References

1. Mitamura K et al (2020) Determination of carrier recombination velocity at inclined grain boundaries in multicrystalline silicon through photoluminescence imaging and carrier simulation. J Appl Phys 128(12):125103
2. Lee GH, Rhee CK, Lim KS (2006) A study on the fabrication of polycrystalline Si wafer by direct casting for solar cell substrate. Solar Energy 80(2):220–225
3. Helmreich D (1980) Current aspects of silicon casting. in Proc. Symp. on Electronic and Optical Properties of Polycrystalline or Impure Semiconductors. Electrochemical Society Princeton, NJ
4. Chen L, Dai B (2012) Optimization of power consumption on silicon directional solidification system by using numerical simulations. J Cryst Growth 354(1):86–92

5. Rao S et al (2020) Numerical and experimental investigation of sectional heater for improving multi-crystalline silicon ingot quality for solar cells. J Crystal Growth 537:125606
6. Wu B et al (2008) Bulk multicrystalline silicon growth for photovoltaic (PV) application. J Crystal Growth 310(7–9):2178–2184
7. Linke D et al (2014) Characterization of a 75 kg multicrystalline Si ingot grown in a KRISTMAG®-type G2-sized directional solidification furnace. Solar Energy Mat Solar Cells 130:652–660
8. Gan C et al (2016) Natural sedimentation of insoluble particles during directional solidification of upgraded metallurgical-grade silicon. J Crystal Growth 439:74–79
9. Yuan J et al (2023) The Study of Dislocation Propagation in Si Wafer during IGBT High Thermal Budget Process. in 2023 7th IEEE Electron Devices Technology & Manufacturing Conference (EDTM). IEEE
10. He L et al (2021) Numerical and experimental investigation of octagonal thermal field for improving multi-crystalline silicon ingot quality. Vacuum 185:110007
11. Lau Jr V, Chiang P-t, Lan C-w (2021) In situ visualization of silicon wafer casting on silicon carbide as low nucleation undercooling substrate. J Crystal Growth. **566**. 126142
12. Wu B, et al (2009) Simulation of silicon casting process for photovoltaic (PV) application. in Proceedings of the 2009 TMS Annual Meeting & Exhibition
13. Fujiwara K et al (2006) Growth of structure-controlled polycrystalline silicon ingots for solar cells by casting. Acta Materialia 54(12):3191–3197
14. Su W et al (2022) Design and numerical optimization of gas guidance system in casting silicon furnace by the orthogonal experiment. Silicon 14(1):301–307
15. Nagarajan SG et al (2019) Influence of additional insulation block on multi-crystalline silicon ingot growth process for PV applications. J Crystal Growth 516:10–16
16. Kesavan V, Srinivasan M, Ramasamy P (2019) The influence of multiple-heaters on the reduction of impurities in mc-Si for directional solidification. Silicon 11:1335–1344
17. Srinivasan M et al (2016) Numerical modelling on stress and dislocation generation in multi-crystalline silicon during directional solidification for PV applications. Electron Mat Lett 12:431–438
18. Sugunraj S et al (2023) Influence of helium gas flow under the retort bottom to control the impurities in grown mc-Si ingot by DS process for photovoltaic application: Numerical simulation. J Crystal Growth 609:127151
19. Keerthivasan T et al (2022) Influence of radiation heat transfer on Mc-Si ingot during directional solidification: a numerical investigation. Silicon 14(18):12085–12094
20. Keerthivasan T et al (2023) The impact on mc-Si ingot grown in a directional solidification furnace by partially replacing the susceptor bottom with an insulation material: A numerical investigation. J Crystal Growth 607:127130
21. Gurusamy A et al (2023) Numerical investigation on modified bottom heater of DS furnace to improve mc-Si Ingot. Silicon 1-12
22. Dezfoli ARA (2022) Design and optimization of complex single heater for Vertical Gradient Freeze (VGF) Grower. J Crystal Growth 127051
23. Tseng I-H et al (2021) Effect of thermal stress on anisotropic grain growth in nano-twinned and un-twinned copper films. Acta Materialia 206:116637
24. Dezfoli ARA (2023) Czochralski (CZ) process modification with cooling tube in the response to market Global silicon shortage. J Crystal Growth 610:127170
25. Dezfoli ARA et al (2017) 3D numerical study of coupled crystallization and carbon segregation during multi-crystalline silicon ingot solidification. Mat Sci Semiconduct Proc 59:76–86
26. Dezfoli ARA et al (2016) Modeling of poly-crystalline silicon ingot crystallization during casting and theoretical suggestion for ingot quality improvement. Mat Sci Semiconduct Proc 53:36–46